Three-dimensional flow of Powell–Eyring nanofluid with heat and mass flux boundary conditions

Tasawar Hayat[1,2], Ikram Ullah[1], Taseer Muhammad[1,†], Ahmed Alsaedi[2], and Sabir Ali Shehzad[3]

[1] *Department of Mathematics, Quaid-I-Azam University, 45320, Islamabad 44000, Pakistan*

[2] *Nonlinear Analysis and Applied Mathematics (NAAM) Research Group, Department of Mathematics, Faculty of Science, King Abdulaziz University, Jeddah 21589, Saudi Arabia*

[3] *Department of Mathematics, Comsats Institute of Information Technology, Sahiwal 57000, Pakistan*

(Received 7 December 2015; revised manuscript received 17 February 2016; published online 31 May 2016)

This article investigates the three-dimensional flow of Powell–Eyring nanofluid with thermophoresis and Brownian motion effects. The energy equation is considered in the presence of thermal radiation. The heat and mass flux conditions are taken into account. Mathematical formulation is carried out through the boundary layer approach. The governing partial differential equations are transformed into the nonlinear ordinary differential equations through suitable variables. The resulting nonlinear ordinary differential equations have been solved for the series solutions. Effects of emerging physical parameters on the temperature and nanoparticles concentration are plotted and discussed. Numerical values of local Nusselt and Sherwood numbers are computed and examined.

Keywords: three-dimensional flow, Powell–Eyring fluid, nanoparticles, thermal radiation

PACS: 47.15.Cb, 47.50.–d, 47.57.Qk, 78.67.Bf **DOI:** 10.1088/1674-1056/25/7/074701

1. Introduction

The suspension of solid nanoparticles such as Cu, Ag, TiO_2 or Al_2O_3 in the base fluids like ethylene glycol, oil or water is known as nanofluid. An insertion of nanometer-sized metallic particles in the base fluids leads to an increase in the thermal conductivity of the ordinary base fluids. The nanofluids are expected to have better thermal efficiency than the base fluids. Such fluids can be implemented in the processes of electronic cooling equipment, nuclear reactors, transportation, vehicle computers and transformer cooling, cancer therapy, heating and cooling process of energy conversion, etc. Choi[1] performed an experimental study and found that the addition of nanoparticles enhanced the thermal conductivity of the base fluids. Buongiorno[2] provided a mathematical model to explore the effects of thermophoresis and Brownian motion in the flow of nanofluid. The boundary layer flow of nanofluid induced by linearly stretching the surface was addressed by Khan and Pop.[3] They showed that the thermal boundary layer thickness is an increasing function of both thermophoresis and Brownian motion parameters. Makinde and Aziz[4] investigated the boundary layer flow of nanofluid past a stretching sheet with convective boundary condition. They observed that convective heating at the sheet results in higher temperature and rate of heat transfer from the sheet. Mustafa *et al.*[5] discussed the two-dimensional stagnation-point flow of nanofluid towards a stretching sheet. Turkyilmazoglu[6] studied the heat and mass transfer analysis for MHD flow of viscous nanofluid with slip effect. He provided the closed form solutions of velocity, temperature, and concentration profiles. Rashidi *et al.*[7] provided the second law analysis in the steady flow of nanofluid due to a rotating porous disk. Thermal and concentration stratification effects in the boundary layer flow of viscous nanofluid by a vertical plate were addressed by Ibrahim and Makinde.[8] Sheikholeslami *et al.*[9] explored the MHD flow of nanofluid between two horizontal parallel plates in a rotating system. The flow of viscous nanofluid between the concentric cylinders is discussed by Zeeshan *et al.*[10] Marangoni convection flow and heat transfer in pseudoplastic nanofluids is investigated by Lin *et al.*[11] The MHD flow and heat transfer of nanofluids in porous media with variable surface heat flux, radiation and chemical reaction is examined by Zhang *et al.*[12] Recently, Hayat *et al.*[13] examined the three-dimensional flow of second grade nanofluid in the presence of thermal radiation, chemical reaction, and heat source/sink effects. Here, the flow is caused due to an exponential stretching sheet.

The study of boundary layer flow induced by a stretching surface has gained considerable attention due to its applications in industries and technological processes. There are several examples of such applications which include extrusion of plastic sheets, drawing of plastic films, paper production, wire drawing, hot rolling, metal spinning, and glass blowing. There are many fluids in our daily life usage like certain oils, shampoos, sugar solution, tomato paste, mud, apple sauce, soaps, blood at low shear rate, chyme, personal care products and many others which do not satisfy the Newton's law of viscosity. Such fluids fall into the category of non-Newtonian fluids. In view of the diverse characteristics of these fluids, many models of non-Newtonian fluids have been proposed in the literature. The Powell–Eyring fluid model[14–20] is one of

†Corresponding author. E-mail: taseer_qau@yahoo.com

© 2016 Chinese Physical Society and IOP Publishing Ltd

such models. This model has important features because its constitutive equations can be deduced from the kinetic theory of gases rather than the empirical relation as in the power-law model. Further, it can correctly reduce to Newtonian flow behavior for low and high shear rates, whereas the power-law model describes an infinite effective viscosity for low shear rate and thus limiting its range of applicability.

In the present analysis, we considered the three-dimensional boundary layer flow of Powell–Eyring nanofluid over a bidirectional stretching surface in the presence of thermal radiation. Prescribed surface heat flux and prescribed surface mass flux conditions are utilized at the surface. To the best of the authors' knowledge, all the previous studies discussed the heat transfer through prescribed surface heat flux condition. There is not a single study in nanofluid dynamics that dealt with both the conditions. The main purpose here is to utilize such conditions in the three-dimensional boundary layer flow of Powell–Eyring nanofluid. Mathematical formulation of the present analysis is performed subject to both prescribed surface heat flux and prescribed surface mass flux conditions. The homotopy analysis method (HAM)[21–29] is applied for the solution's development. Temperature and nanoparticles' concentration profiles are examined through the plots. The local Nusselt and local Sherwood numbers are computed numerically and analyzed.

2. Mathematical formulation

Consider the laminar steady three-dimensional boundary layer flow of an incompressible Powell–Eyring nanofluid over a linear stretching surface. The flow is caused by a bidirectional stretching surface. Brownian motion and thermophoresis are taken into account. We consider the Cartesian coordinate system in such a manner that the sheet coincides with the xy-plane and the fluid occupies the space $z \geq 0$. Let $U_{\rm w}(x) = ax$ and $V_{\rm w}(y) = by$ denote the surface stretching velocities along the x- and y-directions respectively (see Fig. 1). The Rosseland's approximation is employed for the thermal radiation expression. The prescribed heat and mass flux conditions are imposed at the boundary. The thermophysical properties of fluid are taken as constant. The governing boundary layer equations of Powell–Eyring nanofluid are

$$\frac{\partial u}{\partial x}+\frac{\partial v}{\partial y}+\frac{\partial w}{\partial z}=0, \tag{1}$$

$$u\frac{\partial u}{\partial x}+v\frac{\partial u}{\partial y}+w\frac{\partial u}{\partial z} = \left(\nu+\frac{1}{\beta d_1\rho}\right)\frac{\partial^2 u}{\partial z^2}-\frac{1}{2\beta\rho d_1^3}\left(\frac{\partial u}{\partial z}\right)^2\frac{\partial^2 u}{\partial z^2}, \tag{2}$$

$$u\frac{\partial v}{\partial x}+v\frac{\partial v}{\partial y}+w\frac{\partial v}{\partial z} = \left(\nu+\frac{1}{\beta d_1\rho}\right)\frac{\partial^2 v}{\partial z^2}-\frac{1}{2\beta\rho d_1^3}\left(\frac{\partial v}{\partial z}\right)^2\frac{\partial^2 v}{\partial z^2}, \tag{3}$$

$$u\frac{\partial T}{\partial x}+v\frac{\partial T}{\partial y}+w\frac{\partial T}{\partial z} = \alpha_{\rm m}\frac{\partial^2 T}{\partial z^2}+\frac{(\rho c)_{\rm p}}{(\rho c)_{\rm f}}\left(D_{\rm B}\left(\frac{\partial T}{\partial z}\frac{\partial C}{\partial z}\right)+\frac{D_{\rm T}}{T_\infty}\left(\frac{\partial T}{\partial z}\right)^2\right) -\frac{1}{(\rho c)_{\rm f}}\frac{\partial q_{\rm r}}{\partial z}, \tag{4}$$

$$u\frac{\partial C}{\partial x}+v\frac{\partial C}{\partial y}+w\frac{\partial C}{\partial z}=D_{\rm B}\frac{\partial^2 C}{\partial z^2}+\frac{D_{\rm T}}{T_\infty}\left(\frac{\partial^2 T}{\partial z^2}\right). \tag{5}$$

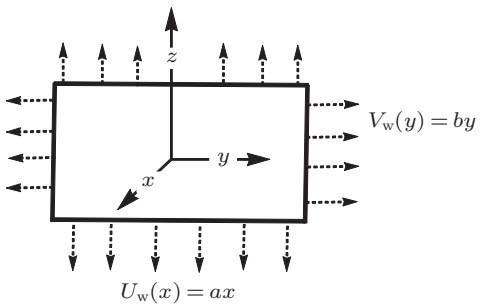


Fig. 1. Geometry of the problem.

The boundary conditions for the present flow analysis are

$$u=ax,\quad v=by,\quad w=0,\quad -k\left(\frac{\partial T}{\partial z}\right)=q_{\rm w},$$

$$-D_{\rm B}\left(\frac{\partial C}{\partial z}\right)=j_{\rm w},\ \text{at}\ z=0, \tag{6}$$

$$u\to 0,\ v\to 0,\ T\to T_\infty, C\to C_\infty,\ \text{as}\ z\to\infty, \tag{7}$$

where u, v, and w are the velocity components in the x, y, and z directions, respectively, $\nu=\mu/\rho$ is the kinematic viscosity, μ is the dynamic viscosity, ρ is the density, $\alpha_{\rm m}=k/(\rho c)_{\rm f}$ is the thermal diffusivity of the fluid, k is the thermal conductivity, $(\rho c)_{\rm f}$ is the heat capacity of fluid, $q_{\rm r}$ is the radiative heat flux, $(\rho c)_{\rm p}$ is the effective heat capacity of nanoparticles, $D_{\rm B}$ is the Brownian diffusion coefficient, T is the temperature, C is the nanoparticles' concentration, $D_{\rm T}$ is the thermophoretic diffusion, $q_{\rm w}$ is the heat flux, $j_{\rm w}$ is the mass flux, a and b are the positive constants, and T_∞ and C_∞ are the temperature and nanoparticles' concentration far away from the surface. The radiative heat flux $q_{\rm r}$ via Rosseland's approximation is given by

$$q_{\rm r}=-\frac{4\delta^*}{3m}\frac{\partial(T^4)}{\partial z}, \tag{8}$$

in which δ^* is the Stefan–Boltzman constant and m is the mean absorption coefficient. We assume that the difference in temperature within the flow is such that T^4 can be written as a linear combination of temperature. By employing a Taylor's series and ignoring higher order terms, we have

$$T^4\cong -3T_\infty^4+4T_\infty^3 T. \tag{9}$$

By inserting Eq. (9) in Eq. (8), we obtain

$$\frac{\partial q_{\rm r}}{\partial z}=-\frac{16\delta^* T_\infty^3}{3m}\frac{\partial^2 T}{\partial z^2}. \tag{10}$$

Substituting Eq. (10) into Eq. (4), we have

$$\begin{aligned} & u\frac{\partial T}{\partial x}+v\frac{\partial T}{\partial y}+w\frac{\partial T}{\partial z} \\ = & \alpha_{\mathrm{m}}\frac{\partial^2 T}{\partial z^2}+\frac{(\rho c)_{\mathrm{p}}}{(\rho c)_{\mathrm{f}}}\left(D_{\mathrm{B}}\left(\frac{\partial T}{\partial z}\frac{\partial C}{\partial z}\right)+\frac{D_{\mathrm{T}}}{T_\infty}\left(\frac{\partial T}{\partial z}\right)^2\right) \\ & +\frac{16\delta^* T_\infty^3}{3m(\rho c)_{\mathrm{f}}}\frac{\partial^2 T}{\partial z^2}. \end{aligned} \tag{11}$$

We now consider the following transformations:

$$\begin{aligned} & u=axf'(\eta),\quad v=ayg'(\eta),\quad w=-(a\nu)^{1/2}(f+g), \\ & T=T_\infty+\sqrt{\frac{\nu}{a}}\frac{q_{\mathrm{w}}}{k}\theta(\eta), \\ & C=C_\infty+\sqrt{\frac{\nu}{a}}\frac{j_{\mathrm{w}}}{D_{\mathrm{B}}}\phi(\eta),\quad \eta=\left(\frac{a}{\nu}\right)^{1/2}z. \end{aligned} \tag{12}$$

Now, equation (1) is automatically satisfied, and equations (2)–(7) and (11) yield

$$(1+\varepsilon)f'''+(f+g)f''-f'^2-\varepsilon\delta_1 f''^2 f'''=0, \tag{13}$$

$$(1+\varepsilon)g'''+(f+g)g''-g'^2-\varepsilon\delta_2 g''^2 g'''=0, \tag{14}$$

$$(1+Rd)\theta''+Pr((f+g)\theta'+N_{\mathrm{b}}\theta'\phi'+N_{\mathrm{t}}\theta'^2)=0, \tag{15}$$

$$\phi''+LePr(f+g)\phi'+\frac{N_{\mathrm{t}}}{N_{\mathrm{b}}}\theta''=0, \tag{16}$$

$$f=0,\ \ g=0,\ \ f'=1,\ \ g'=\alpha, \\ \theta'=-1,\ \ \phi'=-1,\ \ \text{at}\ \ \eta=0, \tag{17}$$

$$f'\to 0,\ \ g'\to 0,\ \ \theta\to 0,\ \ \phi\to 0,\ \ \text{as}\ \ \eta\to\infty. \tag{18}$$

In the above expressions, ε, δ_1, and δ_2 are the Powell–Eyring fluid parameters, α is the ratio parameter, Rd is the radiation parameter, Pr is the Prandtl number, N_{b} is the Brownian motion parameter, N_{t} is the thermophoresis parameter, Le is the Lewis number, and prime stands for differentiation with respect to η. These parameters can be expressed as follows:

$$\begin{aligned} & \varepsilon=\frac{1}{\beta d_1\rho},\quad \delta_1=\frac{a^3x^2}{2\nu d_1^2},\quad \delta_2=\frac{a^3y^2}{2\nu d_1^2}, \\ & \alpha=\frac{b}{a},\quad Rd=\frac{16\delta^* T_\infty^3}{3km}, \\ & Pr=\frac{\nu}{\alpha_{\mathrm{m}}},\quad N_{\mathrm{b}}=\frac{(\rho c)_{\mathrm{p}}D_{\mathrm{B}}(C_{\mathrm{w}}-C_\infty)}{(\rho c)_{\mathrm{f}}\nu}, \\ & N_{\mathrm{t}}=\frac{(\rho c)_{\mathrm{p}}D_{\mathrm{T}}(T_{\mathrm{w}}-T_\infty)}{(\rho c)_{\mathrm{f}}\nu T_\infty},\quad Le=\frac{\alpha_{\mathrm{m}}}{D_{\mathrm{B}}}. \end{aligned} \tag{19}$$

The dimensionless form of local Nusselt number Nu_x and local Sherwood number Sh_x are given by

$$\begin{aligned} & (Re_x)^{-1/2}Nu_x=(1+Rd)\left(\frac{1}{\theta(0)}\right), \\ & (Re_x)^{-1/2}Sh_x=\frac{1}{\phi(0)}, \end{aligned} \tag{20}$$

where $Re_x=ux/\nu$ is the local Reynolds number.

3. Series solutions

The initial guesses and auxiliary linear operators for homotopic solutions are

$$\begin{aligned} & f_0(\eta)=1-\mathrm{e}^{-\eta},\quad g_0(\eta)=\alpha(1-\mathrm{e}^{-\eta}), \\ & \theta_0(\eta)=\mathrm{e}^{-\eta},\quad \phi_0(\eta)=\mathrm{e}^{-\eta}, \end{aligned} \tag{21}$$

$$\begin{aligned} & L_f=f'''-f',\quad L_g=g'''-g', \\ & L_\theta=\theta''-\theta,\quad L_\phi=\phi''-\phi. \end{aligned} \tag{22}$$

The above operators have the following properties:

$$\begin{aligned} & L_f\left[C_1+C_2\mathrm{e}^{\eta}+C_3\mathrm{e}^{-\eta}\right]=0,\quad L_g\left[C_4+C_5\mathrm{e}^{\eta}+C_6\mathrm{e}^{-\eta}\right]=0, \\ & L_\theta\left[C_7\mathrm{e}^{\eta}+C_8\mathrm{e}^{-\eta}\right]=0,\quad L_\phi\left[C_9\mathrm{e}^{\eta}+C_{10}\mathrm{e}^{-\eta}\right]=0, \end{aligned} \tag{23}$$

in which C_i $(i=1-10)$ are arbitrary constants. The zeroth-order problems are defined as follows:

$$\begin{aligned} & (1-p)L_f\left[\hat{f}(\eta,p)-f_0(\eta)\right] \\ = & p\hbar_{\mathrm{f}}N_{\mathrm{f}}[\hat{f}(\eta,p),\hat{g}(\eta,p)], \end{aligned} \tag{24}$$

$$\begin{aligned} & (1-p)L_g\left[\hat{g}(\eta,p)-g_0(\eta)\right] \\ = & p\hbar_g N_g[\hat{f}(\eta,p),\hat{g}(\eta,p)], \end{aligned} \tag{25}$$

$$\begin{aligned} & (1-p)L_\theta\left[\hat{\theta}(\eta,p)-\theta_0(\eta)\right] \\ = & p\hbar_\theta N_\theta[\hat{f}(\eta,p),\hat{g}(\eta,p),\hat{\theta}(\eta,p),\hat{\phi}(\eta,p)], \end{aligned} \tag{26}$$

$$\begin{aligned} & (1-p)L_\phi\left[\hat{\phi}(\eta,p)-\phi_0(\eta)\right] \\ = & p\hbar_\phi N_\phi[\hat{f}(\eta,p),\hat{g}(\eta,p),\hat{\theta}(\eta,p),\hat{\phi}(\eta,p)], \end{aligned} \tag{27}$$

$$\hat{f}(0,p)=0,\quad \hat{f}'(0,p)=1,\quad \hat{f}'(\infty,p)=0, \\ \hat{g}(0,p)=0,\quad \hat{g}'(0,p)=\alpha, \tag{28}$$

$$\hat{g}'(\infty,p)=0,\quad \hat{\theta}'(0,p)=-1,\quad \hat{\theta}(\infty,p)=0, \\ \hat{\phi}'(0,p)=-1,\quad \hat{\phi}(\infty,p)=0, \tag{29}$$

$$\begin{aligned} & N_f\left[\hat{f}(\eta;p),\hat{g}(\eta;p)\right] \\ = & (1+\varepsilon)\frac{\partial^3\hat{f}}{\partial\eta^3}+(\hat{f}+\hat{g})\frac{\partial^2\hat{f}}{\partial\eta^2}-\left(\frac{\partial\hat{f}}{\partial\eta}\right)^2 \\ & -\varepsilon\delta_1\left(\frac{\partial^2\hat{f}}{\partial\eta^2}\right)^2\frac{\partial^3\hat{f}}{\partial\eta^3}, \end{aligned} \tag{30}$$

$$\begin{aligned} & N_g\left[\hat{g}(\eta;p),\hat{f}(\eta;p)\right] \\ = & (1+\varepsilon)\frac{\partial^3\hat{g}}{\partial\eta^3}+(\hat{f}+\hat{g})\frac{\partial^2\hat{g}}{\partial\eta^2}-\left(\frac{\partial\hat{g}}{\partial\eta}\right)^2 \\ & -\varepsilon\delta_2\left(\frac{\partial^2\hat{g}}{\partial\eta^2}\right)^2\frac{\partial^3\hat{g}}{\partial\eta^3}, \end{aligned} \tag{31}$$

$$\begin{aligned} & N_\theta\left[\hat{\theta}(\eta,p),\hat{\phi}(\eta,p),\hat{f}(\eta;p),\hat{g}(\eta;p)\right] \\ = & (1+Rd)\frac{\partial^2\hat{\theta}}{\partial\eta^2}+Pr(\hat{f}+\hat{g})\frac{\partial\hat{\theta}}{\partial\eta} \\ & +PrN_{\mathrm{b}}\frac{\partial\hat{\theta}}{\partial\eta}\frac{\partial\hat{\phi}}{\partial\eta}+PrN_{\mathrm{t}}\left(\frac{\partial\hat{\theta}}{\partial\eta}\right)^2, \end{aligned} \tag{32}$$

$$\begin{aligned} & N_\phi[\hat{\phi}(\eta,p),\hat{\theta}(\eta,p),\hat{f}(\eta;p),\hat{g}(\eta;p)] \\ = & \frac{\partial^2\hat{\phi}}{\partial\eta^2}+LePr(\hat{f}+\hat{g})\frac{\partial\hat{\phi}}{\partial\eta}+\frac{N_{\mathrm{t}}}{N_{\mathrm{b}}}\frac{\partial^2\hat{\theta}}{\partial\eta^2}. \end{aligned} \tag{33}$$

Here, p denotes the embedding parameter, $\hbar_f$, $\hbar_g$, $\hbar_\theta$, and $\hbar_\phi$ the non-zero auxiliary parameters and N_f, N_g, N_θ, and N_ϕ the nonlinear operators. Setting $p=0$ and $p=1$, we have

$$\hat{f}(\eta;0)=f_0(\eta),\quad \hat{g}(\eta;0)=g_0(\eta),$$
$$\hat{\theta}(\eta,0)=\theta_0(\eta),\quad \hat{\phi}(\eta,0)=\phi_0(\eta), \tag{34}$$
$$\hat{f}(\eta;1)=f(\eta),\quad \hat{g}(\eta;1)=g(\eta),$$
$$\hat{\theta}(\eta,1)=\theta(\eta),\quad \hat{\phi}(\eta,1)=\phi(\eta). \tag{35}$$

When p varies from 0 to 1 then $\hat{f}(\eta;p)$, $\hat{g}(\eta;p)$, $\hat{\theta}(\eta,p)$, and $\hat{\phi}(\eta,p)$ vary from the initial guesses $f_0(\eta)$, $g_0(\eta)$, $\theta_0(\eta)$, and $\phi_0(\eta)$ to the final solutions $f(\eta)$, $g(\eta)$, $\theta(\eta)$, and $\phi(\eta)$, respectively. The Taylor series expansion gives the following expressions:

$$\hat{f}(\eta;p)=f_0(\eta)+\sum_{m=1}^{\infty}f_m(\eta)p^m,$$
$$f_m(\eta)=\frac{1}{m!}\frac{\partial^m\hat{f}(\eta,p)}{\partial p^m}\bigg|_{p=0}, \tag{36}$$
$$\hat{g}(\eta;p)=g_0(\eta)+\sum_{m=1}^{\infty}g_m(\eta)p^m,$$
$$g_m(\eta)=\frac{1}{m!}\frac{\partial^m\hat{g}(\eta,p)}{\partial p^m}\bigg|_{p=0}, \tag{37}$$
$$\hat{\theta}(\eta,p)=\theta_0(\eta)+\sum_{m=1}^{\infty}\theta_m(\eta)p^m,$$
$$\theta_m(\eta)=\frac{1}{m!}\frac{\partial^m\hat{\theta}(\eta,p)}{\partial p^m}\bigg|_{p=0}, \tag{38}$$
$$\hat{\phi}(\eta,p)=\phi_0(\eta)+\sum_{m=1}^{\infty}\phi_m(\eta)p^m,$$
$$\phi_m(\eta)=\frac{1}{m!}\frac{\partial^m\hat{\phi}(\eta,p)}{\partial p^m}\bigg|_{p=0}. \tag{39}$$

The convergence of the above series strongly depends upon $\hbar_f$, $\hbar_g$, $\hbar_\theta$, and $\hbar_\phi$. Considering that $\hbar_f$, $\hbar_g$, $\hbar_\theta$, and $\hbar_\phi$ are chosen in such a manner that Eqs. (36)–(39) converge at $p=1$ then we have

$$f(\eta)=f_0(\eta)+\sum_{m=1}^{\infty}f_m(\eta), \tag{40}$$
$$g(\eta)=g_0(\eta)+\sum_{m=1}^{\infty}g_m(\eta), \tag{41}$$
$$\theta(\eta)=\theta_0(\eta)+\sum_{m=1}^{\infty}\theta_m(\eta), \tag{42}$$
$$\phi(\eta)=\phi_0(\eta)+\sum_{m=1}^{\infty}\phi_m(\eta). \tag{43}$$

The mth-order problems have the solutions

$$f_m(\eta)=f_m^*(\eta)+C_1+C_2\,\mathrm{e}^{\eta}+C_3\,\mathrm{e}^{-\eta}, \tag{44}$$
$$g_m(\eta)=g_m^*(\eta)+C_4+C_5\,\mathrm{e}^{\eta}+C_6\,\mathrm{e}^{-\eta}, \tag{45}$$
$$\theta_m(\eta)=\theta_m^*(\eta)+C_7\,\mathrm{e}^{\eta}+C_8\,\mathrm{e}^{-\eta}, \tag{46}$$
$$\phi_m(\eta)=\phi_m^*(\eta)+C_9\,\mathrm{e}^{\eta}+C_{10}\,\mathrm{e}^{-\eta}, \tag{47}$$

in which $f_m^*(\eta)$, $g_{\mathrm{m}}^*(\eta)$, $\theta_m^*(\eta)$, and $\phi_m^*(\eta)$ denote the special solutions.

4. Convergence analysis

Equations (40)–(43) depend upon the non-zero auxiliary parameters $\hbar_f$, $\hbar_g$, $\hbar_\theta$, and $\hbar_\phi$ which play a vital role in controlling and adjusting the convergence of the series solutions. For this purpose, we sketched the $\hbar$-curves at 21st order of approximations that give us the proper ranges of these auxiliary parameters. Figures 2 and 3 show that the suitable ranges of these auxiliary parameters are $-1.6\le\hbar_f\le-0.1$, $-1.5\le\hbar_g\le-0.1$, $-1.4\le\hbar_\theta\le-0.2$, and $-1.35\le\hbar_\phi\le-0.7$. Further, the presented series solutions are convergent in the whole domain of η when $\hbar_f=-0.8=\hbar_g$ and $\hbar_\theta=-0.9=\hbar_\phi$. Table 1 shows that the 34th order of deformations are sufficient for the convergent series solutions.

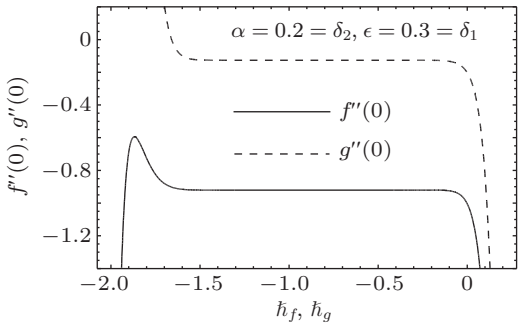


Fig. 2. The $\hbar$-curves for the functions $f(\eta)$ and $g(\eta)$.

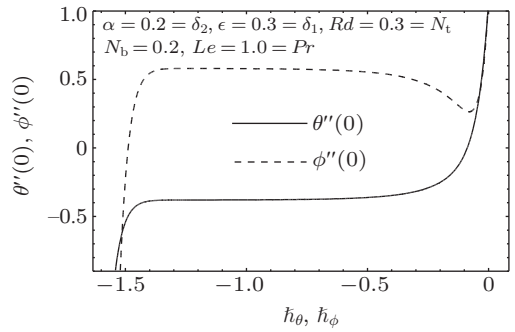


Fig. 3. The $\hbar$-curves for the functions $\theta(\eta)$ and $\phi(\eta)$.

Table 1. Convergence of series solutions for different order of deformations when $Rd=\varepsilon=0.3=\delta_1=N_{\mathrm{t}}$, $Pr=1.0=Le$, and $\alpha=0.2=\delta_2=N_{\mathrm{b}}$.

Order of approximations	$-f''(0)$	$-g''(0)$	$-\theta''(0)$	$\phi''(0)$
1	0.9246	0.1388	0.0650	0.1600
5	0.9247	0.1303	0.2969	0.4692
10	0.9247	0.1303	0.3614	0.5519
15	0.9247	0.1303	0.3766	0.5662
25	0.9247	0.1303	0.3834	0.5752
34	0.9247	0.1303	0.3844	0.5766
45	0.9247	0.1303	0.3844	0.5766
60	0.9247	0.1303	0.3844	0.5766

5. Discussion

The effects of emerging physical parameters namely fluid parameter ε, ratio parameter α, radiation parameter Rd, Prandtl number Pr, thermophoresis parameter N_t, and Brownian motion parameter N_b on the temperature profile $\theta(\eta)$ are shown in Figs. 4–9. Influence of fluid parameter ε on the temperature profile is analyzed in Fig. 4. From Fig. 4, it is noted that the temperature profile $\theta(\eta)$ and thermal boundary thickness are reduced when we increase the values of fluid parameter. Figure 5 shows the impact of ratio parameter α on the temperature profile $\theta(\eta)$. It can be seen that an increase in the ratio parameter reduces the temperature profile $\theta(\eta)$. From Fig. 6, it is observed that the temperature $\theta(\eta)$ and thermal boundary layer thickness are enhanced by the increase in radiation parameter Rd. For $Rd = 0$, there is no thermal radiation effects. Hence, the presence of thermal radiation enhances the temperature and thermal boundary layer thickness. An increase in Prandtl number Pr is observed from Fig. 7. The larger Prandtl number has a relatively lower thermal diffusivity. Therefore, a rapid increase in the Prandtl number Pr reduces the temperature and thermal boundary layer thickness. The influences of thermophoresis and Brownian motion parameters on the temperature profile $\theta(\eta)$ are shown in Figs. 8 and 9. An increase in the thermophoresis and Brownian motion parameters gives rise to the temperature and thermal boundary layer thickness. The presence of nanoparticles greatly enhances the thermal conductivity of the fluid. Here, the thermal conductivity of fluid is enhanced when we increase the values of thermophoresis and Brownian motion parameters. Such increase in thermal conductivity is responsible for the higher temperature and thicker thermal boundary layer thickness.

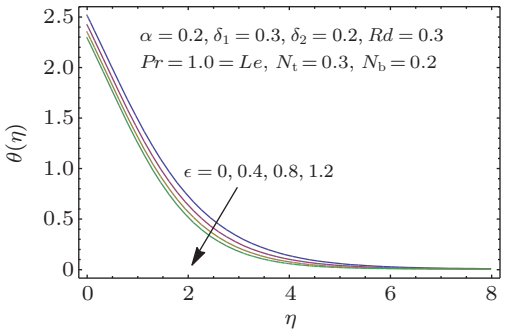


Fig. 4. Impact of ε on $\theta(\eta)$.

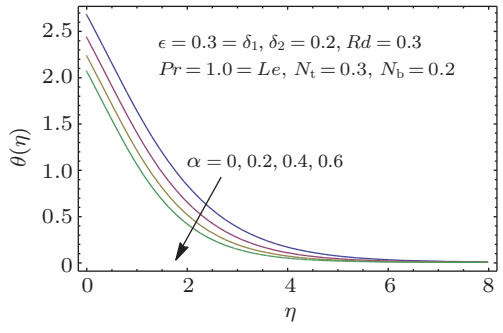


Fig. 5. Impact of α on $\theta(\eta)$.

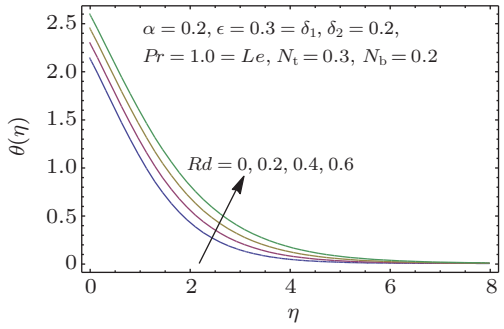


Fig. 6. Impact of Rd on $\theta(\eta)$.

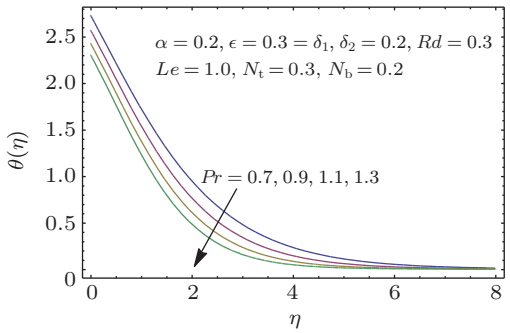


Fig. 7. Impact of Pr on $\theta(\eta)$.

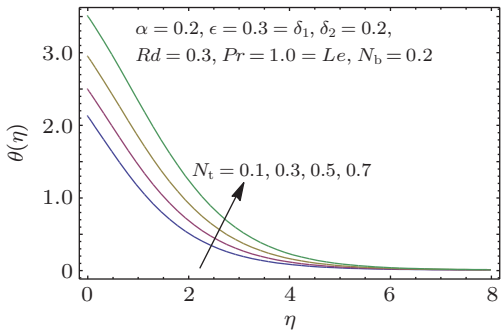


Fig. 8. Impact of N_t on $\theta(\eta)$.

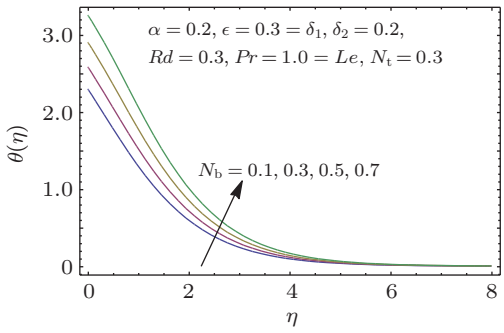


Fig. 9. Impact of N_b on $\theta(\eta)$.

Figures 10–15 are sketched to explore the behavior of fluid parameter ε, ratio parameter α, Lewis number Le, Prandtl number Pr, thermophoresis parameter N_t, and Brownian motion parameter N_b on the nanoparticles concentration profile $\phi(\eta)$. From Fig. 10, it is noticed that the larger values of fluid parameter ε reduce the nanoparticles concentration field $\phi(\eta)$ and its related boundary layer thickness. It is clearly shown that both nanoparticles' concentration $\phi(\eta)$ and its associated boundary layer thickness are reduced for larger values of ratio parameter α (see Fig. 11). Figure 12 is drawn to see the impact of Lewis number Le on the nanoparticles' concentration profile $\phi(\eta)$. The Lewis number is inversely proportional to the Brownian diffusion coefficient due to which an increase in the Lewis number Le yields a decrease in Brownian diffusion coefficient, which results in a decrease in nanoparticles' concentration and its related boundary layer thickness. Nanoparticles' concentration profile $\phi(\eta)$ for different values of Prandtl number Pr is shown in Fig. 13. It is seen that the nanoparticles' concentration profile $\phi(\eta)$ is a decreasing function of Prandtl number Pr. Figure 14 illustrates the variation of nanoparticles' concentration $\phi(\eta)$ for various values of thermophoresis parameter N_t. It is examined that the nanoparticles' concentration boundary layer thickness increases with the increasing value of N_t. Figure 15 displays the effect of Brownian motion parameter N_b on nanoparticles' concentration $\phi(\eta)$. Large N_b leads to an increase in the nanoparticles' motion and consequently the viscosity of nanofluid decreases. That is why the nanoparticles' concentration and its related boundary layer thickness reduces.

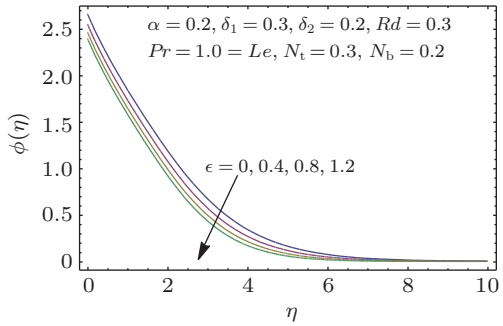


Fig. 10. Impact of ε on $\phi(\eta)$.

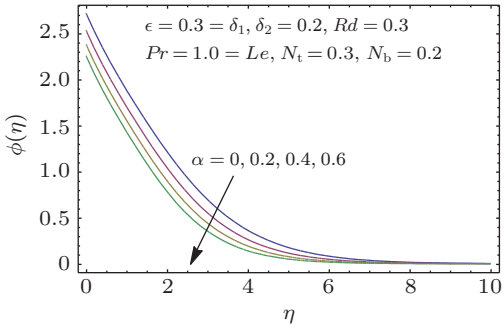


Fig. 11. Impact of α on $\phi(\eta)$.

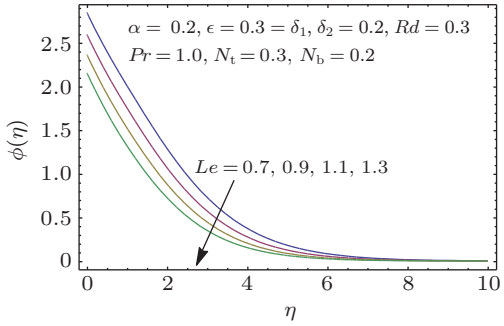


Fig. 12. Impact of Le on $\phi(\eta)$.

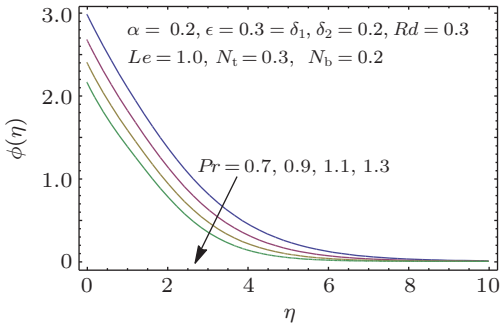


Fig. 13. Impact of Pr on $\phi(\eta)$.

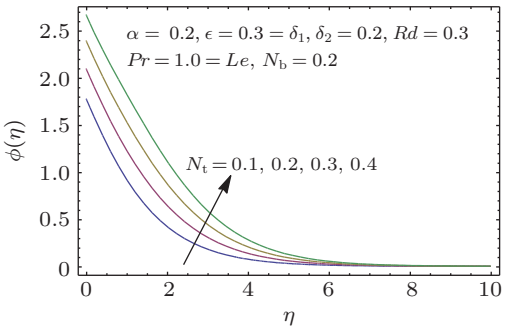


Fig. 14. Impact of N_t on $\phi(\eta)$.

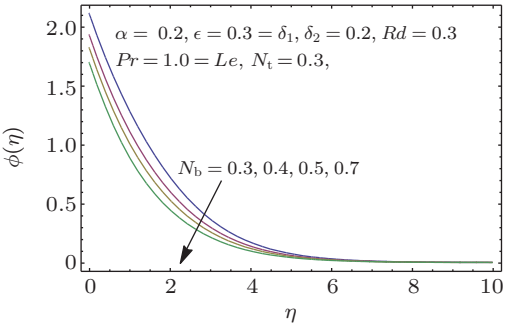


Fig. 15. Impact of N_b on $\phi(\eta)$.

The numerical values of $-f''(0)$, $-g''(0)$, $-\theta''(0)$, and $\phi''(0)$ at different orders of approximations when $Rd = \varepsilon = 0.3 = \delta_1 = N_t$, $\delta_2 = \alpha = 0.2 = N_b$, $Le = 1.0 = Pr$, $\hbar_f = -0.8 = \hbar_g$, and $\hbar_\theta = -0.9 = \hbar_\phi$ are computed in Table 1. This table depicts that the values of $-f''(0)$, $-g''(0)$, $-\theta''(0)$,

and $\phi''(0)$ started to repeat from 34th order of deformations. Therefore, 34th order of approximations are essential for convergent series solutions. Table 2 presents the comparison for various values of ratio parameter with homotopy perturbation method (HPM) and exact solutions. Table 2 shows an excellent agreement of HAM solutions with the existing homotopy perturbation method (HPM) and exact solutions in a limiting sense. This confirms the validity of HAM solutions. Table 3 shows the numerical values of local Nusselt and local Sherwood numbers for various values of δ_1, δ_2, ε, α, Rd, Le, Pr, N_t, and N_b. We have seen that the values of local Nusselt and Sherwood numbers are higher when the larger values of ratio parameter α and radiation parameter Rd are taken into account. An increase in the values of thermophoresis parameter N_t leads to lesser values of local Nusselt and Sherwood numbers.

Table 2. Comparative values of $-f''(0)$ and $-g''(0)$ for various values of α when $\varepsilon = \delta_1 = \delta_2 = 0$.

α	$-f''(0)$			$-g''(0)$		
	HAM	HPM[30]	Exact[30]	HAM	HPM[30]	Exact[30]
0	1	1	1	0	0	0
0.1	1.020260	1.017027	1.020260	0.066847	0.073099	0.066847
0.2	1.039495	1.034587	1.039495	0.148737	0.158231	0.148737
0.3	1.057955	1.052470	1.057955	0.243359	0.254347	0.243360
0.4	1.075788	1.070529	1.075788	0.349209	0.360599	0.349209
0.5	1.093095	1.088662	1.093095	0.465205	0.476290	0.465205
0.6	1.109947	1.106797	1.109947	0.590529	0.600833	0.590529
0.7	1.126398	1.124882	1.126398	0.724532	0.733730	0.724532
0.8	1.142489	1.142879	1.142489	0.866683	0.874551	0.866683
0.9	1.158255	1.160762	1.158254	1.016540	1.022922	1.016539
1.0	1.173722	1.178511	1.173721	1.173722	1.178511	1.173721

Table 3. Values of local Nusselt number $(Re_x)^{-1/2} Nu_x$ and local Sherwood number $(Re_x)^{-1/2} Su_x$ for different values of the parameters ε, δ_1, δ_2, α, Rd, Le, Pr, N_t, and N_b.

ε	δ_1	δ_2	α	Rd	Le	Pr	N_t	N_b	$(Re_x)^{-1/2} Nu_x$	$(Re_x)^{-1/2} Su_x$
0.0	0.3	0.2	0.2	0.3	1.0	1.0	0.3	0.2	0.4423	0.3485
0.5									0.4956	0.3862
1.2									0.5390	0.4181
0.3	0.1	0.2	0.2	0.3	1.0	1.0	0.3	0.2	0.4859	0.3680
	0.3								0.4777	0.3733
	0.5								0.4770	0.3728
0.3	0.3	0.1	0.2	0.3	1.0	1.0	0.3	0.2	0.4773	0.3732
		0.8							0.4773	0.3732
		1.4							0.4773	0.3732
0.3	0.3	0.2	0.0	0.3	1.0	1.0	0.3	0.2	0.4001	0.3352
			0.4						0.5429	0.4047
			0.6						0.6010	0.4323
0.3	0.3	0.2	0.2	0.0	1.0	1.0	0.3	0.2	0.4093	0.3731
				0.5					0.5158	0.3734
				0.8					0.5496	0.3736
0.3	0.3	0.2	0.2	0.3	0.9	1.0	0.3	0.2	0.4745	0.3431
					1.4				0.4880	0.4860
					1.6				0.4922	0.5387
0.3	0.3	0.2	0.2	0.3	1.0	0.7	0.3	0.2	0.3932	0.2803
						0.9			0.4520	0.3431
						1.5			0.5761	0.5133
0.3	0.3	0.2	0.2	0.3	1.0	1.0	0.2	0.2	0.5356	0.4328
							0.5		0.4184	0.3325
							0.7		0.3575	0.3044
0.3	0.3	0.2	0.2	0.3	1.0	1.0	0.3	0.2	0.5762	0.3132
								0.4	0.4256	0.5628
								0.5	0.3619	0.5980

6. Conclusions

The three-dimensional (3D) boundary layer flow of Powell–Eyring nanofluid in the presence of thermal radiation over a bidirectional stretching surface is investigated. Heat and mass flux conditions are imposed for the present analysis. The main points of this research are listed as follows.

(I) Temperature $\theta(\eta)$ and nanoparticles' concentration $\phi(\eta)$ are reduced with the increase in fluid parameter ε.

(II) An increase in radiation parameter Rd shows an enhancement in temperature profile.

(III) Temperature profile enhances when the values of N_t and N_b are increased.

(IV) Nanoparticles' concentration is reduced for an increase in N_b while it is enhanced with larger values of N_t.

(V) Impact of N_b on local Nusselt and local Sherwood numbers are quite the reverse.

References

[1] Choi S U S 1995 *ASME FED* **231** 99
[2] Buongiorno J 2006 *ASME J. Heat Transfer* **128** 240
[3] Khan W A and Pop I 2010 *Int. J. Heat Mass Transfer* **53** 2477
[4] Makinde O D and Aziz A 2011 *Int. J. Thermal Sci.* **50** 1326
[5] Mustafa M, Hayat T, Pop I, Asghar S and Obaidat S 2011 *Int. J. Heat Mass Transfer* **54** 5588
[6] Turkyilmazoglu M 2012 *Chem. Eng. Sci.* **84** 182
[7] Rashidi M M, Abelman S and Mehr N F 2013 *Int. J. Heat Mass Transfer* **62** 515
[8] Ibrahim W and Makinde O D 2013 *Comput. Fluids* **86** 433
[9] Sheikholeslami M, Abelman S and Ganji D D 2014 *Int. J. Heat Mass Transfer* **79** 212
[10] Zeeshan A, Baig M, Ellahi R and Hayat T 2014 *J. Comp. Theor. Nanosci.* **11** 646
[11] Lin Y, Zheng L and Zhang X 2014 *Int. J. Heat Mass Transfer* **77** 708
[12] Zhang C, Zheng L, Zhang X and Chen G 2015 *Appl. Math. Modell.* **39** 165
[13] Hayat T, Muhammad T, Shehzad S A and Alsaedi A 2015 *AIP Adv.* **5** 017107
[14] Zaman H 2013 *Am. J. Comput. Math.* **3** 313
[15] Mushtaq A, Mustafa M, Hayat T, Rahi M and Alsaedi A 2013 *Z. Naturforsch. A* **68** 791
[16] Jalil M, Asghar S and Imran S M 2013 *Int. J. Heat Mass Transfer* **65** 73
[17] Rosca A V and Pop I 2014 *Int. J. Heat Mass Transfer* **71** 321
[18] Hayat T, Asad S, Mustafa M and Alsaedi A 2014 *Plos One* **9** e103214
[19] Poonia M and Bhargava R 2014 *J. Thermophys. Heat Transfer* **28** 499
[20] Ashraf M B, Hayat T and Alsaedi A 2015 *Eur. Phys. J. Plus* **130** 5
[21] Liao S J 2004 *Appl. Math. Comput.* **147** 499
[22] Abbasbandy S, Hayat T, Alsaedi A and Rashidi M M 2014 *Int. J. Numer. Methods Heat Fluid Flow* **24** 390
[23] Sheikholeslami M, Hatami M and Ganji D D 2014 *J. Mol. Liquids* **194** 30
[24] Hayat T, Imtiaz M, Alsaedi A and Mansoor R 2014 *Chin. Phys. B* **23** 054701
[25] Hayat T, Asad S, Mustafa M and Alsulami H H 2014 *Chin. Phys. B* **23** 084701
[26] Lin Y and Zheng L 2015 *AIP Adv.* **5** 107225
[27] Ellahi R, Hassan M and Zeeshan A 2015 *Int. J. Heat Mass Transfer* **81** 449
[28] Hayat T, Muhammad T, Shehzad S A, Chen G Q and Abbas I A 2015 *J. Magn. Magn. Mater.* **389** 48
[29] Abbasi F M, Mustafa M, Shehzad S A, Alhuthali M S and Hayat T 2016 *Chin. Phys. B* **25** 014701
[30] Ariel P D 2007 *Comput. Math. Appl.* **54** 920